Modeling, characterization, and fabrication of bell-tip microneedle array by diffraction and self-aligned lens effects

Cite as: Appl. Phys. Lett. **119**, 023501 (2021); https://doi.org/10.1063/5.0055073 Submitted: 25 April 2021 • Accepted: 28 June 2021 • Published Online: 12 July 2021

🗓 Jun Ying Tan, 🗓 Albert Kim and 🗓 Jungkwun 'JK' Kim







ARTICLES YOU MAY BE INTERESTED IN

GaN nanorods on V-groove textured Si (111): significant light trapping for photoelectrocatalytic water splitting

Applied Physics Letters 119, 023901 (2021); https://doi.org/10.1063/5.0055685

A 3D-printed microfluidic-enabled hollow microneedle architecture for transdermal drug delivery

Biomicrofluidics 13, 064125 (2019); https://doi.org/10.1063/1.5127778

Stable phosphor-in-glass realizing ultrahigh luminescence efficiency for high-power laser-driven lighting

Applied Physics Letters 119, 023301 (2021); https://doi.org/10.1063/5.0055656





Modeling, characterization, and fabrication of bell-tip microneedle array by diffraction and self-aligned lens effects

Cite as: Appl. Phys. Lett. **119**, 023501 (2021); doi: 10.1063/5.0055073 Submitted: 25 April 2021 · Accepted: 28 June 2021 · Published Online: 12 July 2021







Jun Ying Tan,¹ 🕞 Albert Kim,² 🕞 and Jungkwun 'JK' Kim^{1,a)} 🕞

AFFILIATIONS

¹Department of Electrical and Computer Engineering, Kansas State University, Manhattan, Kansas 66502, USA

ABSTRACT

Microneedle arrays have been proposed in a wide range of biomedical applications, such as transdermal drug delivery and sensing. However, a scalable manufacturing process of precise microneedle fabrication of the microneedle has been challenged. This paper demonstrates UV-lithography-based one-step fabrication of fine-tuned bell-tip microneedles using a combination of light diffraction and the self-aligned lens effect. Microscale photopatterns can derive the predictive diffraction patterns where the higher light intensity at the center of the photopattern solidifies the liquid photoresist and forms a microlens shape in a self-aligned manner. The light through the microlens focuses down to a sharp point to form a conical shape for the body of the microneedle. Then light propagation through the vertex of the cone causes light emission, creating a fine bell-tip. The described light propagation behavior was characterized and explained in terms of the light intensity distribution from the diffraction based on the extended Fresnel–Kirchhoff diffraction model. The optics finite element analysis software was used to verify the light propagation and the intensity distribution. The step-by-step fabrication process was demonstrated using biocompatible photosensitive resins and validated the light attenuation and the cross-linking energy. The 20×20 bell-tip microneedles' array was able to be fabricated from the predicted model. Finally, a microneedle array with various shapes and heights on the same substrate was fabricated by single light exposure, demonstrating numerous achievable shapes using the proposed microneedle fabrication method.

Published under an exclusive license by AIP Publishing. https://doi.org/10.1063/5.0055073

A microneedle-integrated transdermal patch is beneficial for drug delivery over conventional oral administration since oral administration is known for its low efficacy due to gastrointestinal degradation and first-pass metabolism. A microneedle array has been known for a minimal-to-painless administration, and therefore it is a promising candidate to replace the highly invasive and low patient compliant infectious hypodermal injection needle. Several reports already demonstrated the microneedle as a transdermal interface for self-administrative drug delivery or sensing (by taking molecules on or through the skin). Although microneedles can bring major benefits, to date there are only a few practical clinical usages. It is attributed to low yield, lack of high-volume manufacturing capability, inconsistent microneedle shape, and thick backing substrate.

Beyond traditional microneedle fabrication methods (e.g., mold and casting and sol-gel method), a one-step process, such as direct drawing lithography $^{8-10}$ or laser ablation micromachining, $^{11-13}$ has been proposed. However, these methods require expensive equipment, multiple

fabrication processes, and long fabrication time, hindering effective manufacturing. The 3D printing microneedle fabrication method has received increasing attention ever since 3D printers have become widely accessible to the public, and in addition to that, the high-end 3D printers have demonstrated micrometer-scaled structures being printed within hours with high resolution and precision. Several 3D printed microneedles have been reported with high complexity and a high level of customization. As most reports used the stereolithography-based 3D printers for the microneedle fabrication, an inevitable layers' effect on the needle body, a relatively low sharpness at the tip, and one-by-one serial fabrication rather than the parallel batch process, still remain challenging for effective manufacturing. Recently, the UV lithography-based fabrication method was reported as low-cost microneedles' fabrication; ^{19–22} however, the end results show poor microneedle surface quality has impeded the practical use of the microneedles.

To address the current shortcomings in microneedle fabrication, this paper introduces a scalable and precise microneedles fabrication

²Department of Electrical and Computer Engineering, Temple University, Philadelphia, Pennsylvania 19122, USA

a) Author to whom correspondence should be addressed: jkkim1324@ksu.edu

method using UV-light diffraction and self-aligned lens-focusing techniques. A unique bell-tip conical shape as a microneedle formed from a photosensitive resin by diffracted light through the micropattern and a self-formed lens focusing effect. The light diffraction through the micropatterns can be explained using the Fresnel–Kirchhoff diffraction theory. The calculation of the diffracted light intensity distribution is verified with the finite element analysis simulation method. The predicted model is further confirmed by the geometry of the fabricated microneedles. Various microneedle arrays were effectively fabricated, including uniform height bell-tip microneedles and variable height bell-tip microneedles with variable base shapes. The fabrication results show the mass production capability and versatility of the proposed fabrication method.

The general concept of the light propagation and the intensity distribution by the diffraction that forms the microneedle was sequentially described as shown in Fig. 1 (steps $\mathfrak{D}-\mathfrak{G}$). Diffraction occurs when collimated UV light travels through a microsize opening (photopattern). The light that propagates forward exhibits a unique intensity distribution (i.e., Gaussian profile). Suppose this light intensity distribution is exposed to the photosensitive resin placed directly on top of the photopattern. In that case, the liquid state resin starts cross-linking by forming a microlens shape at the center (Fig. 1 \mathfrak{D}). The transition of the liquid-to-solid state of the resin affects the path of the UV light propagation due to the differences in the refractive index at the boundary of liquid and solid-state resin. Combining the microlens and the refractive index change, the incident light converges toward the focal point of the microlens, which results in more vigorous intensity at the central region and thereby forming a cone-like solid microneedle,

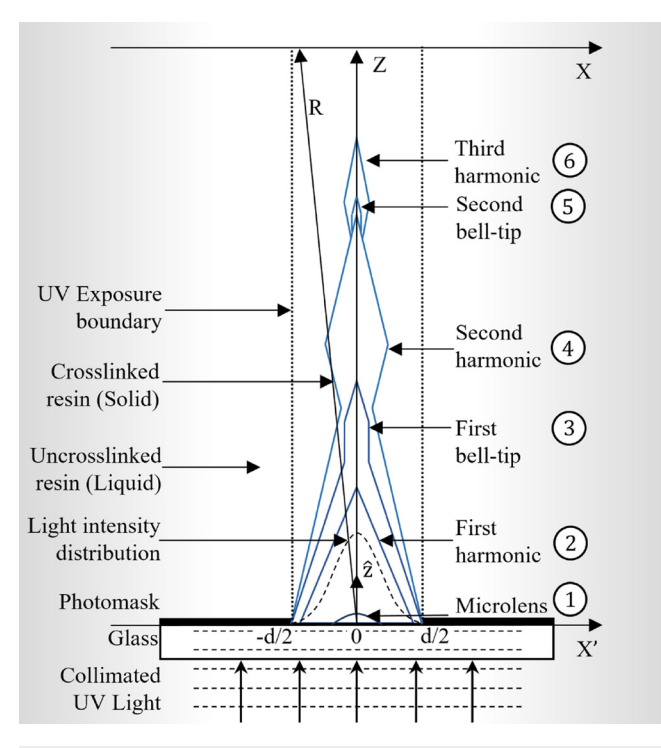


FIG. 1. UV light intensity distribution with a Gaussian profile when passing through a circular photopattern and the microneedle forming sequences.

labeled as the first harmonic (Fig. 1 ②). The additional light energy extends the vertex of the first harmonic and forms the first bell-tip of the microneedle (Fig. 1 ③). The light through the vertex of the first bell-tip diversely propagates due to the diffraction, resulting in the second harmonic (Fig. 1 ④). The same rules continue in the further cross-linking process, which forms the second bell-tip and the third harmonic (Fig. 1 ⑤ and ⑥). The described fabrication principle is also applicable for the hollowed microneedle fabrication by introducing the additional opaque pattern in the middle of the window photopattern in Fig. 1. 23

Diffraction lithography and the intensity distribution of the diffracted light can be explained based on the Fresnel–Kirchhoff diffraction. When the photopattern is assumed circular and symmetrical along the Z-axis, the Fresnel–Kirchhoff diffraction model can be modified for a two-dimensional expression

$$E(x,z) = -\frac{j}{\lambda} \int E(x',0) \frac{e^{jkR}}{R} \left[1 + \frac{\cos(R,\hat{z})}{2} \right] dx', \tag{1}$$

$$R = \sqrt{(x - x')^2 + z^2},\tag{2}$$

where E(x, z) is the field of the diffracted light in the resin and E(x', 0) is the field at any given point on the photopattern. Z is the vertical distance from the photopattern to the resin, λ is the UV light wavelength, and k is the wavenumber. All vectors and parameters are labeled in Fig. 1. The light intensity distribution is expressed by implementing Eq. (1), which can determine the area of the crosslinked resin using the following equation:

$$I(x,z) = \frac{cn\varepsilon_0}{2} \left| E(x,z) \right|^2,\tag{3}$$

where I(x, z) is the intensity in the resin, c is the speed of light, n is the refractive index of the resin, and ε_0 is the free space permittivity.

The Fresnel–Kirchhoff diffraction model is then experimentally validated, as illustrated in the inset of Fig. 2(a). The surgical guide resin (Formlabs, Inc.) was used for the model photosensitive resin. The UV-LED ($\lambda=405\,\mathrm{nm}$; High power UV-LED, Shenzhen Chanzon Technology Co., Ltd.) with a custom-made 3D printed waveguide was used as the source of the collimated UV light. While different thicknesses of the resin (0 to 3000 $\mu\mathrm{m}$) on a glass were exposed to the collimated UV light, the diffracted light intensity on the opposite side was measured using a UV intensity meter (Model 202, G&R Labs Inc.). The measured UV intensity was normalized and presented as the transmission in Fig. 2(a). A fitted curve was generated using the polynomial regression analysis

$$T = \frac{I}{I_0} = 1 - (a_0 + a_1 z - a_0 e^{-a_2 z}), \tag{4}$$

where T is the transmission of the collimated UV light through the resin, I is the measured intensity when the resin height is 0 μ m, z is the resin height, and a_0 , a_1 , and a_2 are the regression constants, where $a_0 = 0.9627$, $a_1 = 0.000\,003\,644$, and $a_2 = 0.002\,878$, in which a_2 is the attenuation factor of the surgical guide resin. The R-squared error of the generated fitted curve was 0.9957, suggesting 99.57% of the generated fitted curve agrees with the measured results. By substituting Eq. (4) in Eq. (3), the intensity of the diffracted light can be rewritten as

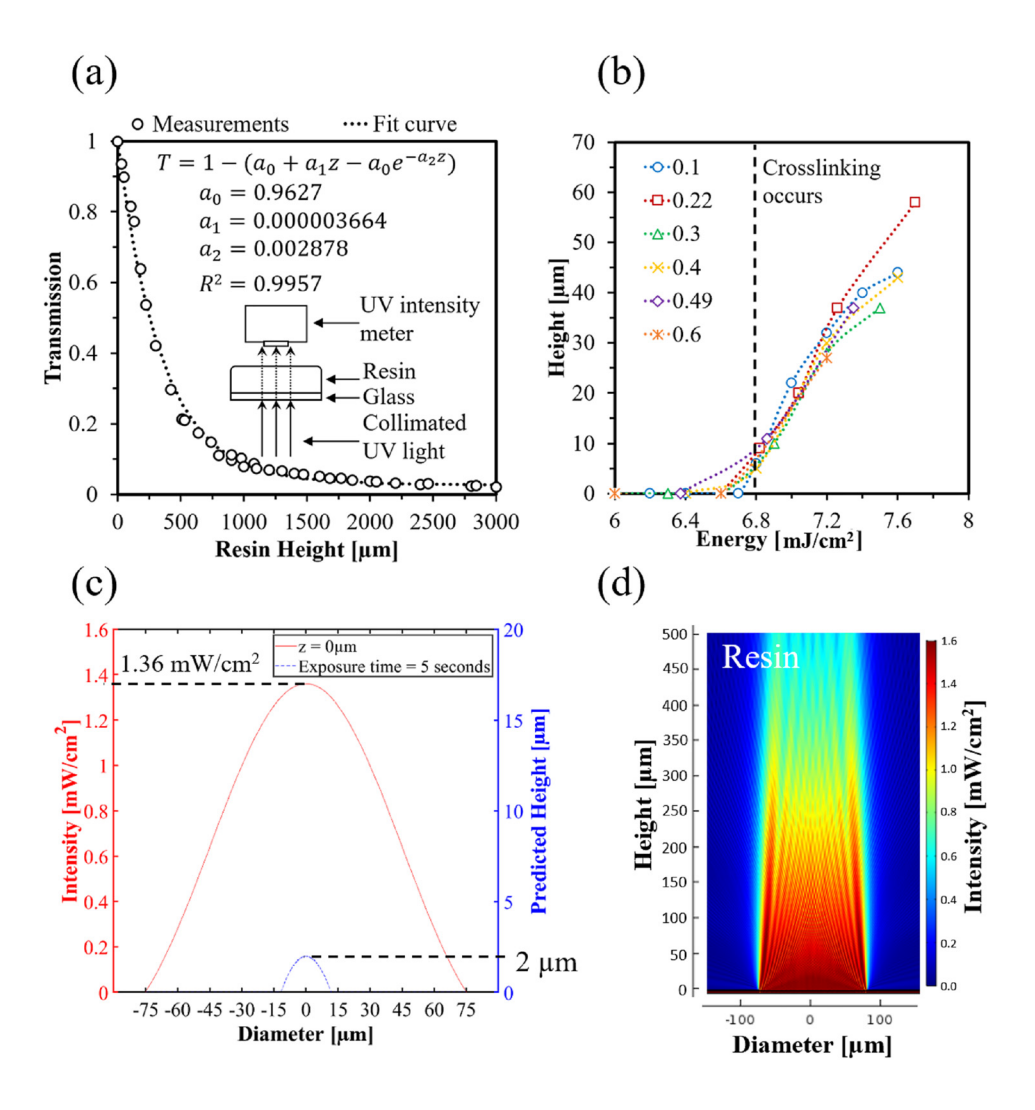


FIG. 2. (a) Measured transmission for 405 nm UV light through various heights of a surgical guide resin and the fit curve generated by the equation with a R-squared error of 99.57%, (b) minimum cross-linking energy of the surgical guide resin for 405 nm UV light, (c) calculated UV intensity on the photopattern based on the Fresnel–Kirchhoff diffraction formula, and (d) simulated UV intensity at t=0 s using COMSOL.

$$I(x,z) = \frac{cn\varepsilon_0}{2} |E(x,z)|^2 [1 - (a_0 + a_1 z - a_0 e^{-a_2 z})].$$
 (5)

The minimum light energy for cross-linking the resin was experimentally verified by investigating the relationship between the applied UV energy and the height of the crosslinked resin. The liquid state resin was coated on a glass substrate and exposed to the collimated 405 nm UV light at various intensities. To precisely monitor the cross-linking response in height, lower light intensities that range from 0.1 to 0.6 mW/cm² were utilized. The heights of the crosslinked resin from various intensities and energies were measured as presented in Fig. 2(b). The minimum cross-linking energy for the surgical guide resin was verified as 6.8 mJ/cm² from the presented data. In this experiment, the surface of the crosslinked resin was assumed as flat, and the secondary reflection of the UV light inside the resin was neglected.

Based on the light intensity distribution in Eqs. (1), (2), and (5) and the experimental data obtained from Figs. 2(a) and 2(b), the overall empirical model was obtained using MATLAB (The MathWorks, Inc.), shown as the red curve in Fig. 2(c). E(x', 0) was assumed to have a Gaussian profile, which was generated using the built-in Bessel

function in MATLAB. The UV intensity was calculated over the diameter of the photopattern (-75 to $75\,\mu m$) at $z\cong 0\,\mu m$. The peak of the diffracted light intensity was set to be $1.36~mW/cm^2$ to mimic the measured intensity. Using the adjusted intensity and the measured minimum cross-linking energy, the associated crosslinked resin height and diameter were predicted and plotted as the blue line in Fig. 2(c). When the exposure time was set at 5 s (energy = $6.8~mJ/cm^2$), the predicted height was calculated to be $2\,\mu m$ and diameter to be $24\,\mu m$. This numerical analysis can only model the first sequence (microlens in Fig. 1 ①), and the rest sequence requires further study using simulation and the experimental effort that accounts for the lens effect.

To validate the calculated result, the diffracted light intensity distribution through a circular photopattern was simulated using the optics module of COMSOL Multiphysics[®] Software (COMSOL, Inc.). Based on the two-dimensional system model as shown in Fig. 1, a transparent glass substrate, two chromium layers with a single slit at the center, and liquid and solid-state surgical guide resins were modeled. The 405 nm UV light source was introduced as a plane wave, propagating in the +Z direction. The slit depicted as a photomask

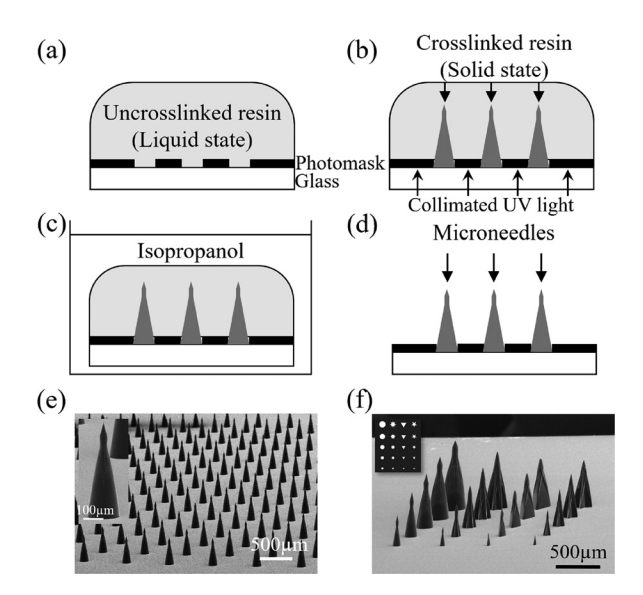


FIG. 3. Fabrication process of the solid microneedles. (a) Coat resin on the photomask, (b) backside UV exposure, (c) develop resin in isopropanol, (d) microneedles complete, (e) 20×20 microneedle array (first bell-tip) with a diameter of $150~\mu m$ and a height of $400~\mu m$, (f) microneedle array with various base shapes (circle, octagonal star, reverse triangle, and pentagonal star) and diameter (100, 150, 200, 250, and $300~\mu m$).

pattern was set to be $150~\mu m$. The liquid and solid-state surgical guide resin refractive indices were set to be 1.46 and 1.5403, respectively. The liquid resin refractive index was acquired through an experiment based on the Snell–Descartes law of refraction, 25 and the solid resin refractive index was acquired from the datasheet. The refractive index of the glass substrate was set to be 1.5. The attenuation factor of the resin was set to be 0.002~878, which was previously derived in Fig. 2(a). The maximum mesh element size was set to be $\lambda/5$. Figure 2(d) shows the simulation results of the diffracted light intensity distribution at t=0~s. The light intensity distribution projected a lenslike shape at the center of the photopattern that enables predicting the initial cross-linking geometry as a microlens. This result is also well aligned with the predicted calculation as presented in Fig. 2(c).

To verify the subsequent diffractive lithography and the microlens effects during the microneedle formation, fabrication was conducted with its corresponding simulation. Figure 3 describes the fabrication process of solid microneedles and SEM images of the fabrication result. The photomask with various photopatterns was prepared where the photomask also served as a substrate. A liquid resin was gently dispensed on the photomask forming a few millimeter thick droplet as depicted in Fig. 3(a). The collimated UV light from a 405 nm UV-LED exposed the backside of the photomask [Fig. 3(b)]. Note that the amount of the exposure energy and the light intensity determines the shape of the microneedle. In this experiment referring to Fig. 3(e) as an example, the light intensities at the LED and the exposure time were 10 mW/cm² and 8 min, respectively. The sample was developed in isopropanol with gentle agitation (20 rpm) for $10 \min [Fig. 3(c)]$. After all the liquid resin is removed, the sample was dried with compressed air to complete the fabrication [Fig. 3(d)]. Figure 3(e) shows an SEM image of a 20×20 first bell-tip microneedles array with high uniformity, demonstrating the batch fabrication capability of the proposed method. The diameter and height of the microneedles in Fig. 3(e) were measured to be 150 and 400 μ m, respectively, suggesting an aspect ratio of 2.67 with a tip size of 2.5 μm and a tip angle of 30°. The designs of the presented microneedles including the aspect ratio have been optimized for skin insertion and mechanical strength against breakage and buckling.²⁷ The similar designs of the presented microneedles with a typical aspect ratio of 2-4 have been generally known for ease of administration, insertion safety, and self-administration via a typical microneedle drug delivery approach such as "poke-and-patch" or "coat-and-poke" without the need for extra equipment.²⁸ However, the proposed method is capable of fabricating over a millimeter tall with a high aspect ratio. To date, the tallest microneedle was fabricated with a height of 1800 μ m with a base diameter of 150 μ m, which has an aspect ratio of 12. Figure 3(f) shows the SEM image of the microneedles array. Each unique microneedle shape was formed by using various photomask patterns that are shown in the inset of Fig. 3(f). Those patterns including circle, octagonal star, reverse triangle, and pentagonal star were incrementally arranged to produce various heights and shapes from the single UV exposure. The diameter of each shape was 100, 150, 200, 250, and 300 μ m resulting in various heights from tens of micrometer to millimeter. The fabrication results demonstrated the process simplicity and the high versatility for the great potential of mass-producing capability as well as highly adaptive to complex microneedles directly applying for 3D organs and skins.

Since the profile of the crosslinked structure is primarily based on the UV light intensity distribution that was affected by the crosslinked structure prior to it, an experiment was conducted to investigate the UV light propagation at various timestamps (5-1200s) and the influence of the current UV light propagation on the later crosslinked structures. The optical images of the crosslinked microneedle structures due to various UV light exposure times (i.e., light energy) are shown in Fig. 4. The surface profiles of the crosslinked structures were outlined using a digital optical microscope (Smartzoom 5, Zeiss, Inc.) and imported into the optics module of COMSOL Multiphysics software to simulate the light propagation through the photopattern and the crosslinked structures (microlens). The light intensity was standardized to be 1.36 mW/cm², and the diameter of the photopattern was 150 μ m throughout the fabrication process. Figure 4(a) shows the first cross-linking that occurs at 5 s, forming the microlens with a height of $2 \mu m$ and a diameter of $24 \mu m$. This result was well agreed with the predicted height and diameter in Fig. 2(c). As seen in the simulated light propagation in insets of Figs. 4(a)-4(c), light converged at the center, demonstrating the self-aligned lens-focusing effect due to the crosslinked structure that is formed in the previous step. This also accelerates the vertical cross-linking rate, resulting in a three times faster height increment than the diameter at the microlens stage. The light propagation simulation shown in Fig. 4(c) also clearly shows that the projected light was converged toward the focal point, which could form the vertex of the first harmonic. Figure 4(d) then confirms the first harmonic at 25 s (energy = 34 mJ/cm^2). The light propagation simulation at this stage visualized the light behavior, which exits the vertex of the first harmonic, converging again at 30 μm above the vertex of the first harmonic before diverging. This behavior of the light formed the first bell-tip at 80 s (energy = 108.8 mJ/cm²), as shown in Fig. 4(e). As the light exiting the first bell-tip, it started to diverge

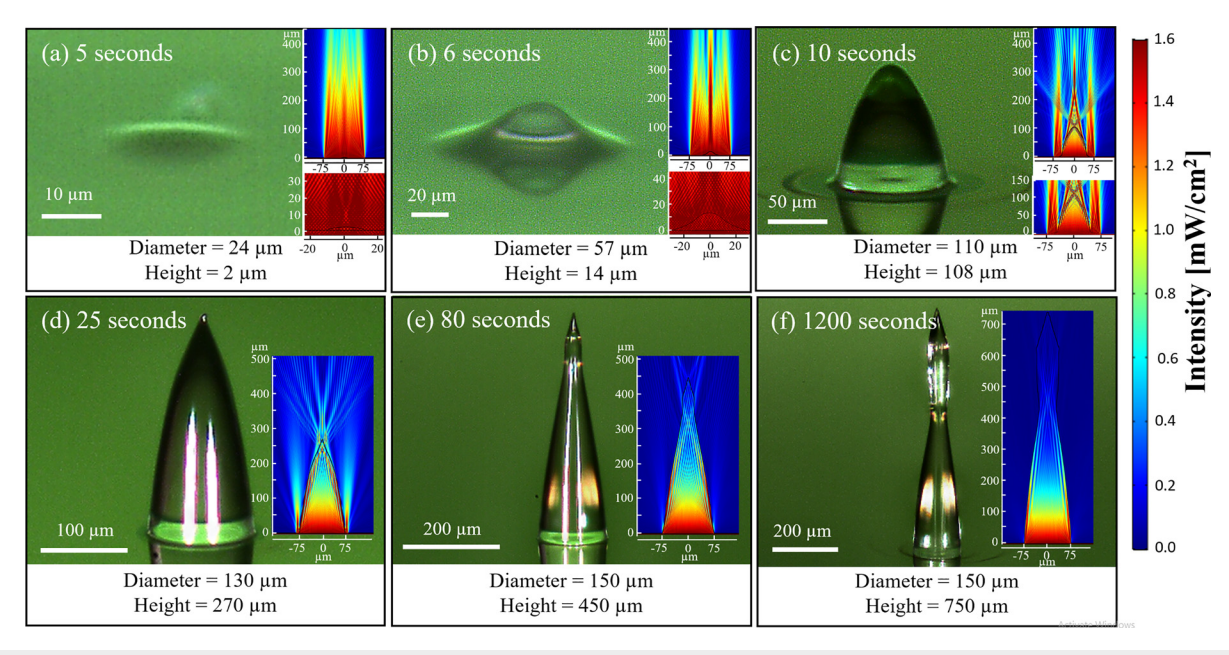


FIG. 4. Transition of the crosslinked resin from the microlens to the microneedle second harmonic and the corresponding UV light propagation. Microlens stage: (a) 5 s, (b) 6 s, and (c) 10 s, microneedle first harmonic stage: (d) 25 s, microneedle first tip stage: (e) 80 s, and microneedle second harmonic stage: (f) 1200 s.

further, as shown in the light propagation simulation in Fig. 4(e). This resulted in the second harmonic at 1200 s [Fig. 4(f)]. The light pattern at the second harmonic [Fig. 4(f)] showed a similar light propagation behavior as the first harmonic [Fig. 4(d)]. It implies that the second bell-tip and third harmonic can be created if sufficient energy was applied. The results of this experiment clearly show that the UV light intensity distribution is the primary factor that determines the later crosslinked structures, which justifies the assumption of this experiment.

In conclusion, we demonstrated a scalable and precise fabrication method for microneedles using diffraction lithography and selfaligned lens-focusing techniques. The light propagation behaviors including the intensity distribution and the diffraction pattern were theoretically calculated using the Fresnel-Kirchhoff diffraction model and verified with the simulation result using COMSOL. Both calculated and simulated results were well matched with the experimental results. A biocompatible surgical guide resin was used for the fabrication of the microneedles. The minimum cross-linking energy and the light attenuation coefficient were obtained as 6.8 mJ/cm² and 0.002 878, respectively. The 20×20 microneedles' array with the first bell-tip was fabricated, showing a uniform measured diameter of 150 μ m, the height of 400 μ m, the aspect ratio of 2.67, a tip size of 2.5 μ m, and a tip angle of 30°. The microneedle array formed by various photopattern base shapes and diameters was also fabricated on a single substrate. Most importantly, the proposed microneedle fabrication technique was a single coating, single UV exposure, and rapid fabrication within 30 minutes, which is expected to provide great potential in microneedle mass production and increase usability in biomedical fields, such as drug delivery application using microneedles.

We acknowledge research grants (Nos. ECCS-2029086 and ECCS-2029077) from the National Science Foundation of the United States.

DATA AVAILABILITY

The data that support the findings of this study are available from the corresponding author upon reasonable request.

REFERENCES

- ¹E. Larrañeta, R. E. M. Lutton, A. D. Woolfson, and R. F. Donnelly, Mater. Sci. Eng. R: Rep. **104**, 1–32 (2016).
- ²A. H. Sabri, Y. Kim, M. Marlow, D. J. Scurr, J. Segal, A. K. Banga, L. Kagan, and J. B. Lee, Adv. Drug Delivery Rev. 153, 195 (2020).
- ³J. H. Park, M. G. Allen, and M. R. Prausnitz, J. Controlled Release 104, 51 (2005).
- ⁴A. Zaid Alkilani, M. T. C. McCrudden, and R. F. Donnelly, Pharmaceutics 7, 438 (2015)
- ⁵B. Yang, X. Fang, and J. Kong, Adv. Funct. Mater. **30**, 2000591 (2020).
- ⁶L. Ventrelli, L. M. Strambini, and G. Barillaro, Adv. Healthcare Mater. 4, 2606 (2015).
- ⁷Y. Yoon, G. S. Lee, K. Yoo, and J. B. Lee, Sensors **13**, 16672 (2013).
- ⁸Z. Xiang, H. Wang, S. K. Murugappan, S. C. Yen, G. Pastorin, and C. Lee, J. Micromech. Microeng. **25**, 025013 (2015).
- ⁹J. Kim, S. Paik, P. Wang, S. Kim, and M. G. Allen, in 2011 IEEE 24th International Conference on Micro Electro Mechanical Systems (IEEE, 2011), pp. 280–283.
- ¹⁰K. Lee and H. Jung, Biomaterials **33**, 7309 (2012).
- ¹¹Y. W. Chen, M. C. Chen, K. W. Wu, and T. Y. Tu, Biomedicines **8**, 427 (2020).
- ¹²S. L. Silvestre, D. Araújo, A. C. Marques, C. Pires, M. Matos, V. Alves, R. Martins, F. Freitas, M. A. M. Reis, and E. Fortunato, ACS Appl. Bio Mater. 3, 5856 (2020).
- ¹³H. R. Nejad, A. Sadeqi, G. Kiaee, and S. Sonkusale, Microsyst. Nanoeng. 4(1), 17073 (2018).
- ¹⁴D. Han, R. S. Morde, S. Mariani, A. A. L. Mattina, E. Vignali, C. Yang, G. Barillaro, and H. Lee, Adv. Funct. Mater. 30, 1909197 (2020).
- ¹⁵K. J. Krieger, N. Bertollo, M. Dangol, J. T. Sheridan, M. M. Lowery, and E. D. O'Cearbhaill, Microsyst. Nanoeng. 5(1), 42 (2019).
- ¹⁶X. Li, W. Shan, Y. Yang, D. Joralmon, Y. Zhu, Y. Chen, Y. Yuan, H. Xu, J. Rong, R. Dai, Q. Nian, Y. Chai, and Y. Chen, Adv. Funct. Mater. 31, 2003725 (2021).

- ¹⁷C. P. P. Pere, S. N. Economidou, G. Lall, C. Ziraud, J. S. Boateng, B. D. Alexander, D. A. Lamprou, and D. Douroumis, Int. J. Pharm. 544, 425 (2018).
- ¹⁸N. El-Sayed, L. Vaut, and M. Schneider, Eur. J. Pharm. Biopharm. 154, 166 (2020).
- 19) Dardano, S. De Martino, M. Battisti, B. Miranda, I. Rea, and L. D. Stefano, Polymers 13, 520 (2021).
- ²⁰H. Takahashi, Y. J. Heo, and I. Shimoyama, J. Microelectromech. Syst. 26, 990 (2017).
- ²¹J. Lim, D. Tahk, J. Yu, D. H. Min, and N. L. Jeon, Microsyst. Nanoeng. 4(1), 29 (2018).
- ²²H. Takahashi, Y. J. Heo, N. Arakawa, T. Kan, K. Matsumoto, R. Kawano, and I. Shimoyama, Microsyst. Nanoeng. 2(1), 16049 (2016).
- ²³J. Y. Tan, A. Kim, and J. Kim, in 2021 21st International Conference on Solid-State Sensors, Actuators and Microsystems (TRANSDUCERS) (2021).
- ²⁴J. W. Goodman, *Introduction to Fourier Optics* (Roberts and Company Publishers, 2005).
- ²⁵E. Rousseau and D. Felbacq, ACS Photonics 7, 1649 (2020).
- 26Formlabs, Surgical guide resin safety data sheet (2019), available at https://formlabs-media.formlabs.com/datasheets/surgical_guide_technical_data_sheet_en.pdf.
- 27S. J. Paik, S. Byun, J. M. Lim, Y. Park, A. Lee, S. Chung, J. Chang, K. Chun, and D. "Dan" Cho, Sens. Actuators, A 114, 276 (2004).
- ²⁸K. van der Maaden, W. Jiskoot, and J. Bouwstra, J. Controlled Release 161, 645 (2012).